SSRG International Journal of Electrical and Electronics Engineering
ISSN: 2348-8379 / https://doi.org/10.14445/23488379/IJEEE-V11I6P102

Volume 11 Issue 6, 12-21, June 2024

Original Article

Investigating the Performance of $A_3B_2X_9$ ($Cs_3Bi_2I_9$) Based Perovskite Photovoltaic Tandem Structure with Crystalline Silicon (c-Si)

Shreyus Goutham Kumar[1], Tadi Surya Teja Reddy[2], N. Suraj[2], C.R. Prashanth[3]

[1]*Department of Electronics and Telecommunication Engineering, Dr. Ambedkar Institute of Technology, Karnataka, India.*
[1,2]*Department of Electronics and Communication Engineering, PES University-EC Campus, Karnataka, India.*
[3]*Department of Electronics and Communication Engineering, SJB Institute of Technology, Affiliated to VTU, Karnataka, India.*

[1]*Corresponding Author : shreyasgouatham@pes.edu*

Received: 01 April 2024 Revised: 03 May 2024 Accepted: 01 June 2024 Published: 29 June 2024

Abstract - *It is now possible for solar cells with a single junction to use organic-inorganic hybrid perovskites that are more than 25.5% efficient. To enhance the device's Power Conversion Efficiency (PCE), one may optimize the absorber layer (perovskite film) or explore innovative device designs like tandem-based solar cells combining perovskite and silicon. By combining perovskite solar cells with silicon solar cells, the overall Power Conversion Efficiency (PCE) may be enhanced beyond the theoretical limit of efficiency for single-junction solar cells, known as the Shockley-Queisser Limit. This is achieved by exploiting a broader spectrum of solar radiation. This study demonstrates the optimization and modeling of a standalone $Cs_3Bi_2I_9$ perovskite solar cell, followed by its integration with a Crystalline-Silicon (c-Si) solar cell to model a tandem structure using the SCAPS-1D numerical simulator. The study aimed to improve the efficiency of a perovskite solar cell by mounting it on a high-efficiency c-Si solar cell utilizing a Four-Terminal (4T) structure. The simulation findings showed that the $Cs_3Bi_2I_9$ perovskite solar cell achieved a power conversion efficiency of 20.37% at a short-circuit current density of 16.165 mA/cm^2 and an open-circuit voltage of 1.41 V. The tandem arrangement showed a power conversion efficiency of 31.59%, greatly surpassing that of individual cells. The modeling findings indicate that the $Cs_3Bi_2I_9$ perovskite solar cell is well-suited for use in tandem systems with c-Si solar cells to achieve high efficiency. This work offers vital insights into creating effective perovskite/c-Si tandem solar cells.*

Keywords - *Perovskite solar cells, Tandem devices, SCAPS 1-D, Power conversion efficiency, Photovoltaic.*

1. Introduction

Several efforts have been made to improve upon single-junction solar cells by constructing multi-junction cells, or tandem cells, which are composed of solar cells with different band gaps. Researchers are still looking into a Shockley-Queisser limit of 31% for single-junction devices. They are looking into it in more detail for a variety of tandem solar device designs, such as multijunction cells with different bandgaps.

This technique is feasible for dealing with the anticipated rise in global energy consumption from 15 TW in 2011 to 30 TW by 2050 [1-3] Utilizing Wide Bandgap (WBG) materials in the top absorber and Narrow Bandgap (NBG) materials in the bottom absorber is suitable for tandem systems. The newest generation of MJ-TSCs used Si as the bottom absorber and III-V compound semiconductor-based materials as the top absorber. Under one sun condition, 39% of the energy had been converted [4].

Expanding in the commercial sector is difficult due to the expensive and precise production needed for III-V compounds. Perovskite materials have influenced research teams exploring III-V materials in the last decade.

Perovskites are seen as potential substitutes due to their advantageous characteristics, including the capacity to modify the bandgap, longer carrier diffusion length, reduced carrier effective mass, improved absorption coefficient, affordability, and simplicity of manufacturing. Research has been conducted on two-junction Tandem Solar Cells (TSCs) to enhance conversion efficiency and reduce the Levelized Cost of Electricity (LCOE) in solar cell technology.

Mailoa et al. developed the first Two-Terminal (2-T) perovskite/Si tandem solar cell in 2015, achieving a Power Conversion Efficiency (PCE) of 13.7% [5]. Zheng et al. enhanced this by using SnO_2 as the Electron Transport Layer (ETL) and Interconnecting Layer (ICL) for the top cell,

achieving a Power Conversion Efficiency (PCE) of 17.10% on 16 cm^2 Tandem Solar Cells (TSC) [6].

The $A_3B_2X_9$ perovskite structure is favored for perovskite solar cell technology due to its unique features. The $A_3B_2X_9$ perovskite structure was favored over the ABX_3 structure for many reasons. The $A_3B_2X_9$ perovskite structure exhibits enhanced energy conversion efficiency due to its increased light absorption capacity. The $A_3B_2X_9$ perovskite structure has a longer carrier lifetime than the ABX_3 structure, enabling it to sustain its energy-conversion efficiency over an extended duration.

The $A_3B_2X_9$ perovskite structure is more stable and less prone to deterioration than the ABX_3 structure. As a result, it is now a more reliable choice for use in perovskite solar cells. The $A_3B_2X_9$ perovskite structure has better defect tolerance compared to the ABX_3 structure, resulting in enhanced performance and greater efficiency. The $A_3B_2X_9$ perovskite structure outperformed the ABX_3 structure in several aspects, including superior light absorption, longer carrier lifespan, stability, and defect tolerance.

The $A_3B_2X_9$ perovskite structure is favored for perovskite solar cells due to its advantages. The $A_3B_2X_9$ perovskite was used as the top cell in tandem perovskite solar cells due to its high light conversion efficiency. The lower cell absorbed low-energy photons, whereas the upper cell absorbed high-energy photons. The tandem construction enables a greater total energy conversion efficiency compared to a single structure.

Bismuth (Bi^{3+}) is a non-toxic element that may replace lead (Pb) in the production of Pb-free perovskites or perovskite-like materials. Park et al. [7] studied the photovoltaic characteristics of Zero-Dimensional (0D) perovskite-type materials such as $Cs_3Bi_2I_9$ and $MA_3Bi_2I_9$ in 2015. Mobin et al. at IIT Indore synthesized a one-dimensional polymeric structure of ($MA_3Bi_2Cl_9$) and used it as a light absorber. However, the final product proved to be inefficient [8].

The reason for this might be the high bandgap of ($MA_3Bi_2Cl_9$), which is 2.85 eV. Significant efforts were made to develop high-performance Pb-free PSCs; however, the Power Conversion Efficiency (PCE) was below 1%. $Cs_3Bi_2I_9$ is an all-inorganic material that exhibits favorable optoelectronic properties and has similarities with perovskite.

We were able to simulate Pb-free PSCs by using the SCAPS-1D program. The device architecture consisting of ($FTO/Cd_{0.5}Zn_{0.5}S/Cs_3Bi_2I_9/CuSbS_2/Au$) was used. Furthermore, in order to make a simulation of the TPSC, we used c-Si as the bottom subcell and the simulated perovskite structure as the top subcell. As far as we know, no one has yet reported a theoretical simulation of Pb-free PSCs ($FTO/Cd_{0.5}Zn_{0.5}S/Cs_3Bi_2I_9/CuSbS_2/Au$) that experiments have backed up.

2. Device Structure

The tandem solar cells' performance was analyzed by simulating the top and bottom sub-cells independently. The tunnel junction was considered to be perfect, and the traditional multi-junction model did not take into account any optical or electrical losses at the interfaces. Perovskite solar cells are often used as the top cells and silicon solar cells as the bottom cells in tandem solar cell configurations, as seen in Figure 1.

The study used a $Cs_3Bi_2I_9$ perovskite solar cell as the top cell, with a band gap of 1.9 eV and a thickness of 1.00 µm, showcasing a high open-circuit Voltage and Absorption Coefficient (VOC). A Hole-Transport Layer (HTL) and Electron-Transport Layer (ETL) sandwich the perovskite layer. $CuSbS_2$ (band-gap: 1.580 µm, thickness: 0.100 µm), the material that makes up the HTL, has great stability and outstanding hole-transport characteristics [9]. $Cd_{0.5}Zn_{0.5}S$ (bandgap: 2.8, thickness: 0.150 µm), which has a narrow bandgap and high electron mobility, was used to fabricate the ETL.

Crystalline Silicon (c-Si) cells, which have high open-circuit voltage, low resistance, and long-term stability, constitute the bottom cell. To ensure that the greatest amount of energy was captured, the bandgap and voltage of the c-Si cell were tuned to match those of the perovskite cell. It is a highly efficient photovoltaic device owing to the combination of the perovskite cell's high absorption coefficient, high open-circuit voltage, low resistance, low bandgap, high electron mobility of the ETL, good hole-transport properties of the HTL, and the low bandgap and high electron mobility of the ETL. The back contact (Au) was used only for standing along the cell. The tandem-structure ETL ($CuSbS_2$) was in contact with n+Si.

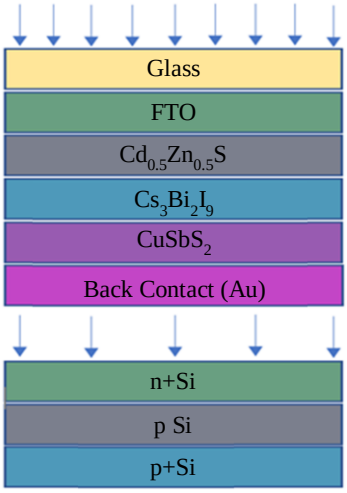

Fig. 1 Structure of proposed standalone and tandem solar cell

3. Methodology

This study used the Solar Cell Capacitance Simulator (SCAPS) software developed by the Department of Electronics and Information Systems (ELIS) at the University of Ghent, Belgium, for numerical simulation. In a tandem perovskite-on-Si solar device, it was believed that there is a perfect tunnel junction with no optical or electrical losses, even though SCAPS-1D is not fully capable of simulating multi-junction solar cells. The tandem device was divided into two separate diodes. The bottom subcell was modeled using the transmitted spectra from the top subcell, while the top subcell was modeled using the conventional sun spectrum. When it comes to modeling tandem cells using SCAPS-1D, this is a common approach that is often followed. The transmitted spectrum from the top subcell to the bottom subcell was computed to approximate the tandem solar cell. The calculation may be performed using the formula provided in Equation 1 [10].

$$S(\lambda) = S_0(\lambda) \cdot exp(\sum_{i=1}^{4} -\alpha_{mat_i}(\lambda) d_{mat_i}) \quad (1)$$

The filtered or transmitted spectrum is denoted as $S(\lambda)$, and the sun spectrum is denoted as $S_0(\lambda)$, 'i' represents the layer number, α (material) is the absorption coefficient of the material, and 'd' is the thickness of the layer in centimeters. It is possible to determine the material's absorption coefficient by using the formula that is shown in Equation 2 [10].

$$\alpha(E) = A_a \cdot \sqrt{h\nu - E_g} \quad (2)$$

Where $A_\alpha = 10^5$ $cm^{-1}eV^{-1/2}$ [11], where 'h' represents the Planck constant in eV.sec, ν is the frequency of the spectrum in sec^{-1}, and E_g is the material's band gap in eV. Figure 2 displays the filtered spectrum of the proposed design. The results of the simulations of the reference PSC using the parameters listed in Table 1 are Voc = 1.22 V, Jsc = 12.19 mA/cm2, FF = 77.73%, and PCE = 11.54% [12].

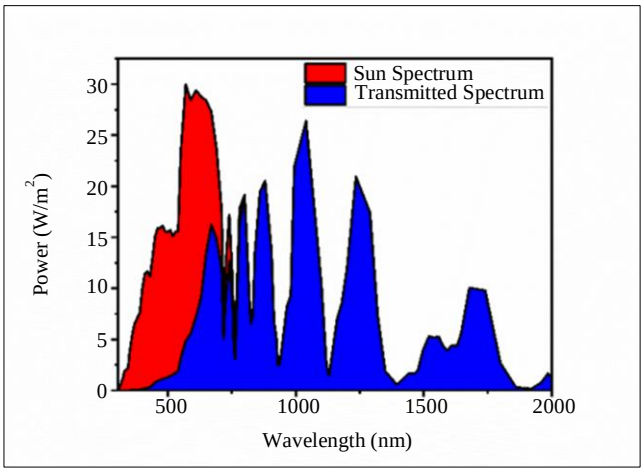

Fig. 2 AM 1.5 sun spectrum with the filtered spectrum from the top sub-cell

Table 1. Simulation parameters of reference PSC

Parameter	FTO	TiO_2	$Cs_3Bi_2I_9$	Spiro-OMeTAD
Thickness (nm)	500	150	650	100
Eg (eV)	3.5	3.2	2.03	3
χ (eV)	4	4.2	3.55	2.2
Er	9	10	9.68	3
N_c (cm^{-3})	$2.2x10^{18}$	$2.2x10^{18}$	$4.98x10^{19}$	$2.2x10^{18}$
N_v (cm^{-3})	$1.8x10^{19}$	$1.8x10^{19}$	$2.11x10^{19}$	$1.8x10^{19}$
μ_e (cm^2 VS^{-1})	20	100	4.3	$2x10^{-4}$
μ_h (cm^2 VS^{-1})	10	25	1.7	$2x10^{-4}$
N_D (cm^{-3})	$2x10^{19}$	$1x10^{19}$	$1x10^{9}$	0
N_A (cm^{-3})	-	0	$1x10^{9}$	$2x10^{18}$
N_t	$1x10^{15}$	$1x10^{15}$	$1x10^{15}$	$1x10^{15}$

By simulating the reference perovskite solar cell with various ETL and HTL materials and changing the thickness, band gap, and total density of defects of the absorber layer/perovskite layer, we were able to optimize it. In this study, we combined these studies with this optimized cell and simulated a tandem solar cell using c-Si as the bottom cell and the optimized cell as the top subcell.

Different ETL materials, such as (IGZO, $Cd_{0.5}Zn_{0.5}S$, CdS, C_{60}, PCBM, AZO, ZnO, and LBSO)[13-18], whose parameters are obtained from various published reports and summarized in Table 2, are used to carry out the simulation using the same methodology as before, in order to obtain the best ETL material to maximize the cell function is maximized.

Table 2. Input parameters for different ETLs

Parameter	IGZO	$Cd_{0.5}Zn_{0.5}S$	CdS	C_{60}	PCBM	AZO	ZnO	LBSO
E_g (eV)	3.05	2.8	2.4	1.7	2	3.3	100	100
χ (eV)	4.16	3.9	4.2	3.9	3.9	3.8	3.3	3.12
ε_r	10	10	10	4.2	3.9	9	4.1	4.4
N_c (cm^{-3})	$5x10^{18}$	$1x10^{18}$	$2.2x10^{18}$	$8\ x10^{19}$	$2.5x10^{21}$	$4\ x10^{18}$	9	22
N_v (cm^{-3})	$5x10^{18}$	$1x10^{18}$	$1.8x10^{19}$	$8\ x10^{19}$	$2.5x10^{21}$	$1x10^{19}$	4×10^{18}	1.8×10^{20}
μ_e ($cm^2\ VS^{-1}$)	15	100	100	0.08	0.2	100	1×10^{19}	1.8×10^{20}
μ_h ($cm^2\ VS^{-1}$)	0.1	25	25	0.0035	0.2	25	100	0.69
N_D (cm^{-3})	$1x10^{18}$	$1x10^{17}$	$1x10^{17}$	$2.6x10^{18}$	$2.93\ x10^{17}$	$1x10^{18}$	50	0.69
N_A (cm^{-3})	0	0	0	0	0	0	1×10^{18}	2×10^{21}
N_t	$1x10^{15}$	$1x10^{15}$	$1x10^{17}$	$1x10^{14}$	$1x10^{15}$	$1x10^{15}$	1×10^{5}	0

The simulation was carried out using the same methodology, substituting several HTL materials such (Cu_2O, CuI, PEDOT: PSS, $CuSbS_2$, NiO, P_3HT, and CuSCN) [9, 13-15, 18] whose parameters were also obtained from various published publications given in Table 3. With the PSC using Spiro-OMeTAD as the HTL and TiO_2 as the ETL, the thicknesses of the various ETL and HTL materials were maintained at 150 and 100 nm, respectively, to check their performance.

Table 3. Input parameters for different HTLs

Parameters	Cu_2O	CuI	CuSCN	NiO	PEDOT: PSS	$CuSbS_2$	P_3HT
E_g (eV)	2.17	2.98	3.4	3.8	2.2	1.58	200
χ (eV)	3.2	2.1	1.9	1.46	2.9	4.2	1.85
ϵ_r	6.6	6.5	10	11.7	3	14.6	3.1
N_c (cm^{-3})	$2.5x10^{20}$	$2.8x10^{19}$	$1.7x10^{19}$	$2.5x10^{20}$	$2.2\ x10^{15}$	$2x10^{18}$	3.4
N_v (cm^{-3})	$2.5\ x10^{20}$	$1x10^{19}$	$2.5x10^{21}$	$2.5x10^{20}$	$1.8\ X10^{18}$	$1x10^{19}$	1×10^{22}
μ_n (cm^2/Vs)	80	0.00017	0.00015	2.8	0.02	49	1×10^{22}
μ_p (cm^2/Vs)	80	0.0002	0.1	2.8	0.0002	49	0.0001
N_d (cm^{-3})	0	0	0	0	0	0	0.001
N_a (cm^{-3})	$1x10^{18}$	$1x10^{18}$	$1x10^{18}$	$1x10^{18}$	$3.17\ x10^{14}$	$1.38x10^{18}$	0
N_t (cm^{-3})	$1x10^{15}$	$1x10^{15}$	$1x10^{14}$	$1x10^{15}$	$1x10^{15}$	$1x10^{14}$	3.1×10^{13}

3.1. Numerical Methods

Recently, simulation treatments for the optimization and evaluation of various parameters have attracted the majority of interest in solar research. Planar heterojunction OIP solar cells were numerically simulated in this study using SCAPS-1D software. The JV curve, power conversion efficiency, projected energy band gap, etc., are performance metrics that can be evaluated using the continuity equation for solving Poisson's equation, as shown in Equations 3 to 5. The PCE, FF, J_{sc}, and V_{oc} were calculated from these curves.

$$\frac{d}{dz}[-\varepsilon(z)\frac{d\emptyset}{dz} = q[p(z) - n(z) + N_D^+(z) - N_A^-(z) + p_t(z) - n_t(z)] \quad (3)$$

$$\frac{dp_n}{dt} = G_p - \frac{p_n - p_{n0}}{\tau_p} + p_n\mu_p\frac{d\xi}{dz} + \mu_p\xi\frac{dp_n}{dz} + D_p\frac{d^2p_n}{dz^2} \quad (4)$$

$$\frac{dn_p}{dt} = G_p - \frac{n_p - n_{p0}}{\tau_n} + n_p\mu_n\frac{d\xi}{dz} + \mu_n\xi\frac{dn_p}{dz} + D_p\frac{d^2n_p}{dz^2} \quad (5)$$

Furthermore, it is important to note that solar cells solely absorb photons with energies greater than the band gaps of semiconductors, resulting in the production of holes and electron pairs. The shortest wavelength of photons with sufficient energy to produce carriers is determined using the equation. Hence, the cutoff wavelength is given by Equation 6.

$$\lambda = \frac{1240}{E_g(eV)} \quad (6)$$

At J= 0 mAcm^{-2}, The highest voltage that a solar cell can generate, known as the open-circuit voltage (Voc), can be represented as shown in Equation 7.

$$V_{oc} = \frac{kT}{q}ln\left(\frac{J_{sc}}{J_0} + 1\right) \quad (7)$$

Where J_o is the saturation point current density, temperature is given by T, q is the carrier charge, and k is Boltzmann's constant. The FF is given by Equation 8.

$$FF = \frac{P_m}{V_{oc} \times J_{sc}} \quad (8)$$

Once more, Green [19] provides a precise calculation for determining the FF as given in Equation 9.

$$FF = \frac{v_{oc} - ln(v_{oc} + 0.72)}{v_{oc} + 1} \quad (9)$$

v_{oc} is the normalized form of V_{oc}, and is given by Equation 10.

$$v_{oc} = \left(\frac{V_{oc}}{V_{th}}\right) \quad (10)$$

The theoretical FF was to be determined in ideal conditions in the current work, however. The largest FF values are obtained from Equation 5, which ignores the resistive losses [19]. Moreover, the maximum power point of a solar cell's power output to power input ratio is expressed as shown in Equation 11.

$$\eta = \frac{P_m}{P_{in} \times A} \quad (11)$$

Where P_{in} denotes the radiation intensity at incidence, and A denotes the area. When the voltage across the solar cell is zero, the short-circuit current is equivalent to the electricity flowing through the cell. It is supplied by and depends on the solar spectrum used, as given in Equation 12.

$$J_{sc} = q\int_{E_g}^{\infty}\frac{dN_{ph}}{dhv}d(hv) \quad (12)$$

The relationship in Equation 13 offers a comprehensive understanding of bandgap changes based on the temperature, T, at any given time.

$$E_g(T) = E_g(0) - \frac{\alpha T^2}{(T+\beta)^2} \quad (13)$$

The constants α and β are primary factors that determine the short-circuit current (J_{sc}). The electron mobility has a significant impact on J_{sc}, and adjusting the material's properties can alter the material-dependent electron affinity, which also plays a vital role.

4. Results and Discussion

A tandem device is comprised of a series of two-cell combinations that form a tandem structure with two terminals. Thus, the open-circuit voltage of the tandem cell Voc is the summation of its subcell voltages. However, the lowest junction current limits the short-circuit current, Jsc, of the entire device [20]. The following section includes a simulation of both the entire tandem device and the individual cells.

4.1. Results and Validation

As discussed in the previous section, the reference PSC with Spiro-OMeTAD and TiO_2 were used as the HTL and ETL materials, respectively. In later sections of this study, we optimized various HTL and ETL materials to select materials that can provide the best device performance. The final proposed structure is shown in Figure 1.

The defect density, bandgap, and thickness of the perovskite layers were optimized. The band gap and defect density ranges were validated using [9, 21] respectively. $Cs_3Bi_2I_9$ was validated using the synthesis process described previously [12, 22, 23].

4.2. Selection of ETL

The function of the electron transport layer is to transport the electrons generated in the absorber layer when sunlight separates them into pairs of electrons and holes and directs them to the front contact of the PSC. Additionally, it hinders holes from moving through the absorber layer and reaching the front contact.

We analyzed the open-circuit voltage, current density, and efficiency of several ETLs using Spiro-OMeTAD as the host material to determine the optimal ETL. The ETLs, such as C_{60}, ZnO, PCBM, IGZO, CdS, AZO, LBSO, and $Cd_{0.5}Zn_{0.5}S$, were evaluated and compared.

Table 4. Simulation results of various ETL materials

	TiO_2	PCBM	$Cd_{0.5}Zn_{0.5}S$	CdS	C_{60}	IGZO	AZO	ZnO	LBSO
Voc	1.36	1.36	1.44	1.36	1.32	1.36	1.43	1.41	1.18
Jsc	12.18	11.98	12.19	12.24	6.13	12.07	12.19	12.18	12.16
FF	68.61	73.51	75.09	62.12	78.20	66.21	74.74	67.82	65.94
PCE	11.43	11.98	13.21	10.35	6.35	10.89	13.06	11.71	9.48

Table 5. Simulation results of various HTL materials

	PEDOT: PSS	NiO	CuSCN	CuI	Cu_2O	$CuSbS_2$	P_3HT
Voc	1.42	1.44	1.43	1.40	1.43	1.43	1.08
Jsc	12.25	12.19	12.19	12.19	12.30	12.17	12.18
FF	38.47	73.63	72.50	68.95	80.33	85.38	34.42
PCE	6.69	12.94	12.72	11.82	14.21	14.89	4.57

Figure 3 illustrates the influence of various ETLs on the PSC. Table 4 displays the physical parameters used in the simulations. Table 4 shows that AZO had the highest open circuit voltage. In contrast, CdS had the maximum current density of 12.24 mA/cm^2 at 1.36 V. AZO and $Cd_{0.5}Zn_{0.5}S$ were the only electron transport layers that achieved efficiency over 13%. Figure 3 illustrates the performance improvement. Due to $Cd_{0.5}Zn_{0.5}S$ having the greatest Power Conversion Efficiency (PCE), we selected it as the optimal layer for the Electron Transport Layer (ETL).

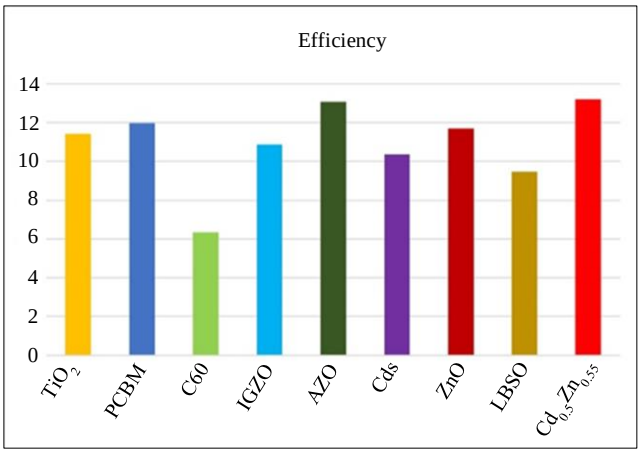

Fig. 3 Efficiency of various ETL materials

enhances solar cell efficiency by facilitating a pathway for the holes to establish electrical contact.

We investigated many HTL materials after selecting the ETL material $Cd_{0.5}Zn_{0.5}S$, such as $CuSbS_2$, CuI, CuSCN, PEDOT, PSS, Cu_2O, NiO, and P3HT. Table 5 indicates that $CuSbS_2$ outperformed the other Hole-Transport Layer (HTL) materials. The device exhibited the greatest Voc of 1.43 V, Jsc of 12.17 mA cm^{-2}, FF of 85.38%, and PCE of 14.89%. Figure 4 displays the efficacy of several HTL layers.

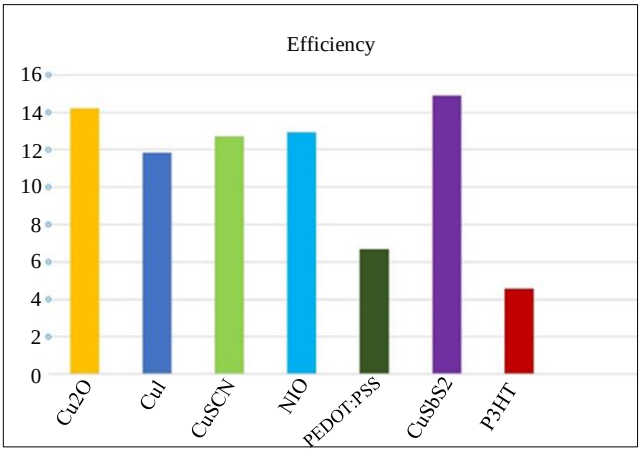

Fig. 4 Efficiency of various HTL Materials

4.3. Selection of HTL

The Hole Transport Layer (HTL) in a solar cell facilitates the transfer of positive charges or holes from the absorber layer to the electrical interface. To enhance the overall performance of the solar cell, the Hole Transport Layer (HTL) may minimize the recombination of holes and electrons at the interface between the light-absorbing layer and the electrical contact. The solar cell's efficiency falls when holes and electrons recombine at the interface since they are then unable to contribute to the current generated by the solar cell. The Hole Transport Layer (HTL) minimizes recombination and

4.4. Effect of Absorber Layer Thickness

The overall cell performance was considerably dependent on the thickness of the perovskite layer. Using numerical simulations, its impact on the overall performance of the cell was also examined. The effects of varying the thickness in the range of 100–2000 nm are shown in Figure 5. The figure shows that the Jsc and PCE values increased with an increase in the perovskite layer thickness, while Voc and FF decreased. More photons were absorbed by the layer with an increase in the thickness of the perovskite layer, increasing the Jsc value. Therefore, an increase in the excess carrier concentration leads

to an increase in Jsc. However, with an increase in the thickness of the perovskite layer, the internal power depletion and series resistance of the solar cell also increase, causing FF and Voc to decrease continuously. As the thickness approached and surpassed 1000 nm, the PCE reached its maximum and then started to decline, as shown in Figure 5.

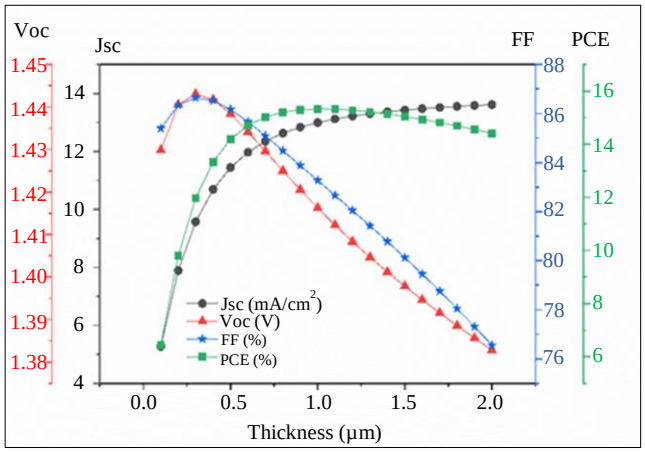

Fig. 5 Effect of thickness of absorber layer

4.5. Effect of Defect Density of Absorber Layer Perovskite Layer

Most of the photogenerated electrons were produced in the perovskite absorber layer. Consequently, the characteristics of the perovskite absorption sheets have a significant impact on cell performance. The quality of the absorption film was significantly affected by the defect density. Compared with the carrier generation rate, absorber layers with a higher defect density perform poorly and have a higher carrier recombination rate [24].

To evaluate the effect of the density of absorber layer defects on the performance of the cell, the performance of PSCs with various defect densities in the perovskite layer was simulated. The defect density measurements in this investigation varied from 10^9 to 10^{13} cm^3 [21]. It is clear from Figure 6 that the PCE and FF decreased as the absorber layer defect density increased.

A nonradiative Shockley-Read-Hall recombination center is a deep energy-level defect. As a result, as the number of defects in the absorber layer increases, charge recombination increases, leading to an increase in Voc and Jsc. At the same time, the short minority carrier lifespan decreases.

Furthermore, the essential p-n junction does not form as the PSC transitions to semi-insulation, resulting in poor cell performance when the absorber defect density is lower than or equal to the doping density. To achieve the best PSC performance, the density of defects in the absorber layer must be decreased, if not eliminated, to achieve the best PSC performance. A substantial reduction in the defect density using current product innovations is still extremely difficult. According to our study, to achieve maximum cell effectiveness, the defect density of the perovskite layer should not exceed 10^{15} cm^{-3}.

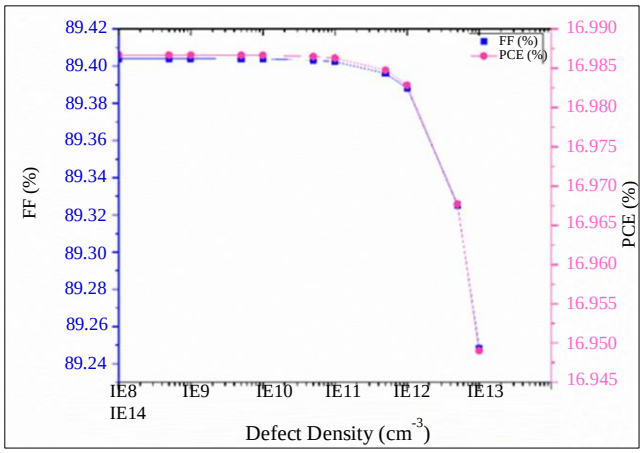

Fig. 6 Effect of defect density

4.6. Effect of Band Gap of Absorber Layer/Perovskite Layer

The band gap of $Cs_3Bi_2I_9$ falls between 1.9 eV and 2.2 eV. We can see from the simulated results presented in Figure 7 that 1.9 eV is the ideal bandgap for high efficiency, as shown in the graph; with an increase in the bandgap, the PCE decreases. Therefore, the bandgap of the absorber layer to 1.9 eV. Temperature is another factor that affects the bandgap of materials. The temperature affects the energy bandgap, which is inversely proportional, as shown in Equation 12.

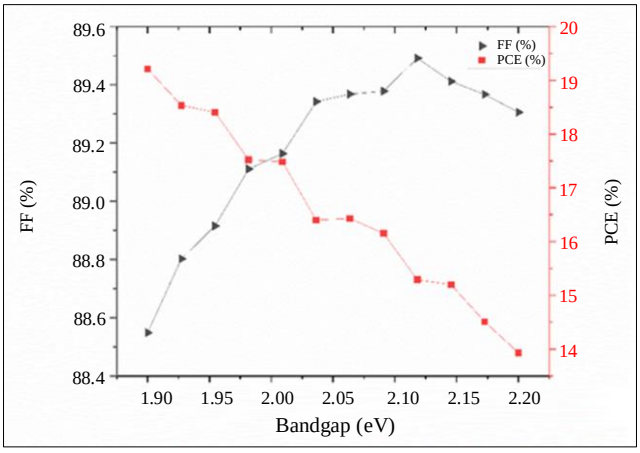

Fig. 7 Effect of band gap

4.7. Simulation of Top Cell (FTO/$Cd_{0.5}Zn_{0.5}S$/$Cs_3Bi_2I_9$/$CuSbS_2$/Au)

Using SCAPS-1D, standalone devices with active layers of $Cs_3Bi_2I_9$ were simulated. The layer thickness of the top device was as follows: the thickness of the active layer (also known as the perovskite layer) was 1000 nm, ETL ($Cd_{0.5}Zn_{0.5}S$) was 150 nm, HTL ($CuSbS_2$) was 100 nm, and ITO layer (FTO) was 500 nm. Table 6 lists the other

parameters used in the simulations. SCAPS - 1D software simulates the standalone top perovskite solar cell using these parameters. According to Table 7, we obtained an efficiency of 20.37% in our simulation. The optimized simulation results of the proposed structure are listed in Table 7. Figure 8 shows the JV characteristics of the standalone top cell.

Table 6. Input parameters for different layers used for SCAPS – 1D simulation

Parameters	FTO	$Cd_{0.5}Zn_{0.5}S$	$Cs_3Bi_2I_9$	$CuSbS_2$	n+Si	p Si	p+Si
Thickness(µm)	0.500	0.150	1	0.100	0.500	300	10
E_g (eV)	3.5	2.8	1.9	1.58	1.12	1.12	1.12
χ (eV)	4	3.9	3.55	4.2	4.05	4.05	4.05
ϵ_r	9	10	9.68	14.6	11.9	11.9	11.9
N_c (cm^{-3})	$2.2x10^{18}$	$1x10^{18}$	$4.98x10^{19}$	$2x10^{18}$	$2.8x10^{19}$	$2.8x10^{19}$	$2.8x10^{19}$
N_v (cm^{-3})	$1.8x10^{19}$	$1x10^{18}$	$2.11x10^{19}$	$1x10^{19}$	$1.04x10^{19}$	$1.04x10^{19}$	$1.04x10^{19}$
μ_n (cm^2/Vs)	20	100	4.3	49	1400	1400	1400
μ_p (cm^2/Vs)	10	25	1.7	49	450	450	450
N_d (cm^{-3})	$2x10^{19}$	$1x10^{17}$	$1x10^{9}$	0	$1x10^{20}$	0	0
N_a (cm^{-3})	-	0	$1x10^{9}$	$1.38x10^{18}$	0	$1x10^{16}$	$1x10^{20}$
N_t (cm^{-3})	$1x10^{15}$	$1x10^{15}$	$1x10^{13}$	$1x10^{15}$	-	-	-

Table 7. Optimized parameters

Optimized Parameters	Optimized Layer / Values	PCE (%)
ETL	$Cd_{0.5}Zn_{0.5}S$	13.21
HTL	$CuSbS_2$	14.89
Absorber Layer Thickness	1.00 µm	15.33
Defect Density of Absorber Layer	1.00E+13	16.95
Band Gap of Absorber Layer	1.9 eV	20.37
Tandem	c-Si (Bottom Cell)	31.59

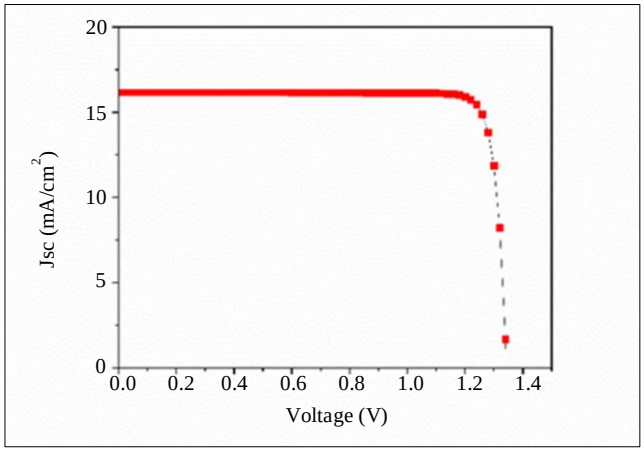

Fig. 8 JV characteristics of the top cell

4.8. Simulation of the Bottom Cell (c-Si)

The bottom cell of the tandem device used in this study is a c-Si solar cell. Here, n+ Si of 0.5 nm, p Si of 300 nm, and p+ Si of 10 nm have been used. The electrical properties of the separate cells must be matched to determine the efficiency of tandem solar cells. This synchronization ensured that the light absorbed by each layer was effectively converted into electrical energy.

The electrical resistance and open-circuit voltage between cells can be matched by modifying the layer thickness, doping levels, and material composition of each layer to achieve current-matching conditions in tandem solar cells. Tandem solar cells are a potential technology for the production of renewable energy because they can achieve high conversion efficiencies by preserving the current matching state. According to Table 8, we obtained an efficiency of 22.78% in our simulation.

4.9. Simulation of Tandem Solar Cell

In mechanically stacked tandem perovskite solar cells, the perovskite top cell is responsible for capturing high-energy photons, whereas the c-Si bottom cell captures lower-energy photons. The perovskite layer is known for its high light-absorption coefficient, fast charge-carrier mobility, and low cost, making it a promising photovoltaic material. The c-Si bottom cell, on the other hand, is a well-established material with a long history of commercialization in the photovoltaic industry. By combining these two materials in a mechanically stacked configuration, tandem perovskite solar cells can

achieve high conversion efficiencies and overcome some of the limitations of single-junction cells. However, the stability and long-term performance of perovskite materials are still under investigation, and the development of stable and scalable fabrication processes is essential for the commercialization of mechanically stacked tandem perovskite solar cells.

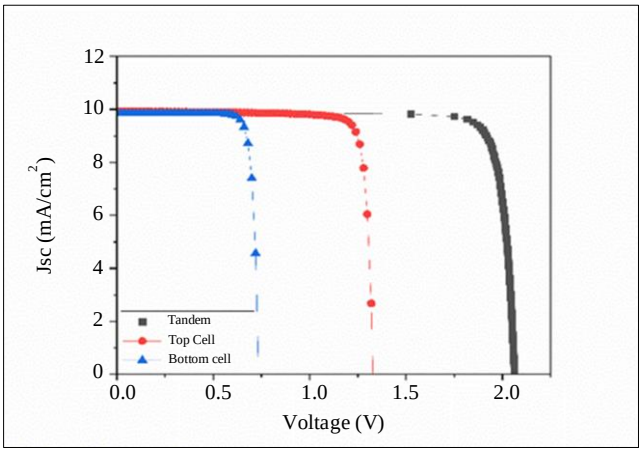

Fig. 9 JV characteristic curve

The tandem cell was simulated using SCAPS-1-D simulation software using the basic method. Mechanically stacked two-terminal tandem cells, which are essentially two diodes connected in series, were used in our analysis, and the current matching condition between the top and bottom cells was also applied. The cell with the lower Jsc dominated the current-limiting criterion of the entire tandem arrangement, even when the voltage was derived by summing the voltages of the individual cells. The maximum power current density (JMP) and Jsc variation were used to match the current. The current-matching profile of the $Cs_3Bi_2I_9$/c-Si tandem structure is shown in Figure 9. We adjusted the bottom cell thickness to determine the current-matching point. As shown in Table 8, we obtained an efficiency of 31.59% was obtained in our simulation.

Table 8. Results of simulations

Cell	Voc	Jsc	FF (%)	PCE (%)
Reference [12]	1.22	12.19	77.73	11.54
$Cs_3Bi_2I_9$ (Top Cell)	1.34	16.14	88.55	20.37
c-Si (Bottom Cell)	0.74	21.28	85.25	22.78
$Cs_3Bi_2I_9$ on c-Si (Tandem)	2.06	9.92	86.07	31.59

5. Conclusion

In this study, non-lead PSCs with an absorber layer composed of $Cs_3Bi_2I_9$ perovskite were investigated using SCAPS modelling. First, it was decided which materials were best for the HTL and ETL: $CuSbS_2$ and $Cd_{0.5}Zn_{0.5}S$, respectively. The effects of the absorber layer thickness, defect density, and bandgap on the PSC performance were then investigated. The PSC setup was a glass substrate/FTO/ $Cd_{0.5}Zn_{0.5}S$/ $Cs_3Bi_2I_9$/$CuSbS_2$/Au. According to modelling studies, the ideal thickness of the absorber layer is 1000 nm. The simulations also concluded that the ideal defect density of the absorber layer is $1x10^{13}$ cm^{-3} and that any higher defect density will result in solar cell performance reduction because additional recombination sites will occur. The findings of this research will contribute to the creation of effective non-lead PSCs and the expansion of solar, wind, wave and other forms of renewable energy.

Acknowledgement

The authors would like to extend their acknowledgement to Gent University, Belgium, for developing and providing the SCAPS-1D simulator used in this work. We want to express our gratitude to the Visvesvaraya Technological University (VTU) for its support and resources that facilitated the completion of this research paper. Also, we would like to thank P.E.S University, Bengaluru, India, for supporting the work.

References

[1] Surbhi Sharma et al., "Waste-to-Energy Nexus for Circular Economy and Environmental Protection: Recent Trends in Hydrogen Energy," *Science of The Total Environment*, vol. 713, 2020. [CrossRef] [Google Scholar] [Publisher Link]

[2] Moritz F. Glatt et al., "Technical Product-Service Systems: Analysis and Reduction of the Cumulative Energy Demand," *Journal of Cleaner Production*, vol. 206, pp. 727-740, 2019. [CrossRef] [Google Scholar] [Publisher Link]

[3] Sukran Seker, and Nezir Aydin, "Hydrogen Production Facility Location Selection for Black Sea Using Entropy Based TOPSIS under IVPF Environment," *International Journal of Hydrogen Energy*, vol. 45, no. 32, pp. 15855-15868, 2020. [CrossRef] [Google Scholar] [Publisher Link]

[4] Martin Green et al., "Solar Cell Efficiency Tables (Version 57)," *Progress in Photovoltaics: Research and Applications*, vol. 29, no. 1, pp. 3-15, 2021. [CrossRef] [Google Scholar] [Publisher Link]

[5] Jonathan P. Mailoa et al., "A 2-Terminal Perovskite/Silicon Multijunction Solar Cell Enabled by a Silicon Tunnel Junction," *Applied Physics Letters*, vol. 106, no. 12, 2015. [CrossRef] [Google Scholar] [Publisher Link]

[6] Jianghui Zheng et al., "Large Area Efficient Interface Layer Free Monolithic Perovskite/Homo-Junction-Silicon Tandem Solar Cell with Over 20% Efficiency," *Energy & Environmental Science*, vol. 11, pp. 2432-2443, 2018. [CrossRef] [Google Scholar] [Publisher Link]

[7] B.W. Park et al., "Bismuth Based Hybrid Perovskites $A_3Bi_2I_9$ (A: Methylammonium or Cesium) for Solar Cell Application," *Advanced Materials*, vol. 27, no. 43, pp. 6806-6813, 2015. [CrossRef] [Google Scholar] [Publisher Link]

[8] Khursheed Ahmad et al., "Design and Synthesis of 1D-Polymeric Chain Based $[(CH_3NH_3)_3Bi_2Cl_9]n$ Perovskite: A New Light Absorber Material for Lead Free Perovskite Solar Cells," *ACS Applied Energy Materials*, vol. 1, no. 6, pp. 2405-2409, 2018. [CrossRef] [Google Scholar] [Publisher Link]

[9] R. Teimouri, and R. Mohammadpour, "Potential Application of $CuSbS_2$ as the Hole Transport Material in Perovskite Solar Cell: A Simulation Study," *Superlattices and Microstructures*, vol. 118, pp. 116-122, 2018. [CrossRef] [Google Scholar] [Publisher Link]

[10] Jihye Gwak Kihwan Kim et al., "Simulations of Chalcopyrite/c-Si Tandem Cells Using SCAPS-1D," *Solar Energy*, vol. 145, pp. 52-58, 2017. [CrossRef] [Google Scholar] [Publisher Link]

[11] Usha Mandadapu, S. Victor Vedanayakam, and K. Thyagarajan, "Simulation and Analysis of Lead based Perovskite Solar Cell Using SCAPS-1D," *Indian Journal of Science and Technology*, vol. 10, no. 11, pp. 1-8, 2017. [CrossRef] [Google Scholar] [Publisher Link]

[12] Khursheed Ahmad et al., "Numerical Simulation and Fabrication of Pb-Free Perovskite Solar Cells (FTO/TiO_2/$Cs_3Bi_2I_9$/spiro-MeOTAD/Au)," *Optical Materials*, vol. 128, 2022. [CrossRef] [Google Scholar] [Publisher Link]

[13] Faisal Baig et al., "Efficiency Enhancement of $CH_3NH_3SnI_3$ Solar Cells by Device Modeling," *Journal of Electronic Materials*, vol. 47, pp. 5275-5282, 2018. [CrossRef] [Google Scholar] [Publisher Link]

[14] Faiza Azri et al., "Electron and Hole Transport Layers Optimization by Numerical Simulation of a Perovskite Solar Cell," *Solar Energy*, vol. 181, pp. 372-378, 2019. [CrossRef] [Google Scholar] [Publisher Link]

[15] Lingyan Lin et al., "A Modeled Perovskite Solar Cell Structure with a Cu_2O Hole-Transporting Layer Enabling over 20% Efficiency by Low-Cost Low-Temperature Processing," *Journal of Physics and Chemistry of Solids*, vol. 124, pp. 205-211, 2019. [CrossRef] [Google Scholar] [Publisher Link]

[16] Nacereddine Lakhdar, and Abdelkader Hima, "Electron Transport Material Effect on Performance of Perovskite Solar Cells Based on $CH_3NH_3GeI_3$," *Optical Materials*, vol. 99, 2020. [CrossRef] [Google Scholar] [Publisher Link]

[17] Ling-yan Lin et al., "Analysis of Sb_2Se_3/CdS Based Photovoltaic Cell: A Numerical Simulation Approach," *Journal of Physics and Chemistry of Solids*, vol. 122, pp. 19-24, 2018. [CrossRef] [Google Scholar] [Publisher Link]

[18] Hsi-Kuei Lin et al., "Dual Nanocomposite Carrier Transport Layers Enhance the Efficiency of Planar Perovskite Photovoltaics," *RSC Advances*, vol. 8, pp. 12526-12534, 2018. [CrossRef] [Google Scholar] [Publisher Link]

[19] Lingyan Lin et al., "A Modeled Perovskite Solar Cell Structure with a Cu_2O Hole-Transporting Layer Enabling over 20% Efficiency by Low-Cost Low-Temperature Processing," *Journal of Physics and Chemistry of Solids*, vol. 124, pp. 205-211, 2019. [CrossRef] [Google Scholar] [Publisher Link]

[20] Thue T. Larsen-Olsen et al., "Roll-to-Roll Processed Polymer Tandem Solar Cells Partially Processed from Water," *Solar Energy Materials and Solar Cells*, vol. 97, pp. 43-49, 2012. [CrossRef] [Google Scholar] [Publisher Link]

[21] Vincent M. Le Corre et al., "Revealing Charge Carrier Mobility and Defect Densities in Metal Halide Perovskites via Space-Charge-Limited Current Measurements," *ACS Energy Letters*, vol. 6, no. 3, pp. 1087-1094, 2021. [CrossRef] [Google Scholar] [Publisher Link]

[22] Arka Sarkar et al., "Synthesis of Ultrathin Few-Layer 2D Nanoplates of Halide Perovskite $Cs_3Bi_2I_9$ and Single-Nanoplate Super-Resolved Fluorescence Microscopy," *Inorganic Chemistry*, vol. 57, no. 24, pp. 15558-15565, 2018. [CrossRef] [Google Scholar] [Publisher Link]

[23] Ravindra Waykar et al., "Environmentally Stable Lead-Free Cesium Bismuth Iodide (Cs3Bi2I9) Perovskite: Synthesis to Solar Cell Application," *Journal of Physics and Chemistry of Solids*, vol. 146, 2020. [CrossRef] [Google Scholar] [Publisher Link]

[24] Hui-Jing Du et al., "Device Simulation of Lead-Free $CH_3NH_3SnI_3$ Perovskite Solar Cells with High Efficiency," *Chinese Physics B*, vol. 25, no. 10, 2016. [CrossRef] [Google Scholar] [Publisher Link]